PAPER

Check for updates

Unraveling Li-ion transport mechanisms in high-entropy anion-disordered argyrodites *via* machine-learned interatomic potentials†

Myeongcho Jang,‡[ab] Kanguk Park,‡[a] Hun-Gi Jung, [ID][acd] Kyung Yoon Chung, [ID][ac] Joon Hyung Shim, [ID]*[b] Ohmin Kwon [ID]*[ae] and Seungho Yu [ID]*[ac]

Lithium argyrodite sulfide solid electrolytes are widely used in all-solid-state batteries owing to their high ionic conductivity. Recently, high-entropy argyrodites formed by anion disorder in Li_6PS_5Cl have emerged as promising superionic conductors. However, the details of the Li-ion conduction mechanism in high-entropy argyrodites have yet to be fully elucidated. In this study, the Li-ion conduction mechanism is systematically investigated through first-principles calculations and molecular dynamics simulations using machine-learned interatomic potentials (MLIPs). The calculations indicate that high-entropy Li_6PS_5Cl argyrodites improve site energy uniformity and facilitate inter-cage jumps, significantly enhancing Li-ion conductivity. Ionic conductivity was further improved with increased disorder in Cl-rich argyrodites, but a critical threshold was observed with the addition of Cl. By leveraging MLIPs, a detailed analysis of the conduction mechanism was efficiently conducted, and a systematic investigation of ionic conductivity through entropy variation was performed. These findings highlight the reliability and effectiveness of MLIPs in facilitating the design and analysis of novel high-entropy superionic argyrodites.

1. Introduction

Li-ion batteries have garnered significant attention as energy storage systems for electric vehicles; however, their limitations in energy density and safety have driven the development of next-generation batteries.[1] All-solid-state batteries (ASSBs) incorporating solid electrolytes (SEs) are widely regarded as among the most promising candidates for next-generation batteries, owing to their combination of high energy density and improved safety.[2,3] ASSBs facilitate the utilization of high-energy-density electrode chemistries, such as metallic Li anodes, anode-less configurations, and thick composite cathodes.[4] Additionally, ASSBs significantly enhance safety by replacing flammable and volatile liquid electrolytes with nonflammable SEs.[5]

Among the various types of SEs, sulfide-based SEs have been widely studied due to their high ionic conductivity, comparable to that of liquid electrolytes.[5,6] Several sulfide SEs, including thio-LISICON-type $Li_{10}GeP_2S_{12}$, glassy $Li_2S–P_2S_5$ type $Li_7P_3S_{11}$, and argyrodite-type $Li_{5.5}PS_{4.5}Cl_{1.5}$, have exhibited high ionic conductivity above 10 mS cm^{-1} at room temperature.[7,8] The lithium argyrodite family, Li_6PS_5X (X = Cl, Br), is regarded as one of the most promising sulfide SEs due to its high ionic conductivity, low cost, and good compatibility in ASSBs.[9,10] Since the discovery of argyrodite SEs in 2008, comprehensive studies have been conducted on their synthesis, ionic conduction mechanisms, structural design, defect chemistry, interfacial stability, and applications in ASSBs.[11–13]

Ionic substitution in argyrodite SEs has significantly enhanced ionic conductivity by facilitating inter-cage jumps for long-range migration.[14] For example, Li vacancy formation through excess halogen anions in Li_6PS_5Cl increased ionic conductivity to approximately 10 mS cm^{-1} for $Li_{5.5}PS_{4.5}Cl_{1.5}$ (cold-pressed state),[15] while anion mixing with Br also enhanced the ionic conductivity.[16–18] Additionally, Li site disorder induced by aliovalent substitution with M^{4+} in $Li_{6+x}M_xP_{1-x}S_5I$ and $Li_{6+x}M_xSb_{1-x}S_5I$ (M = Si, Ge, Sn) significantly enhanced ionic conductivity, achieving 14.8 mS cm^{-1} for $Li_{6.6}Sb_{0.4}Si_{0.6}S_5I$[19] and 16 mS cm^{-1} for $Li_{6.5}Sb_{0.5}Ge_{0.5}S_5I$.[20] Recently, high-entropy argyrodites have been investigated to enhance ion migration through the redistribution of localized ionic sites.[21–25] The

[a]Energy Storage Research Center, Korea Institution of Science and Technology, Seoul 02792, Republic of Korea. E-mail: shyu@kist.re.kr

[b]School of Mechanical Engineering, Korea University, 145 Anam-ro, Seongbuk-gu, Seoul 02841, South Korea. E-mail: shimm@korea.ac.kr

[c]Division of Energy & Environment Technology, KIST School, Korea University of Science and Technology, Seoul 02792, Republic of Korea

[d]Department of Energy Science and KIST-SKKU Carbon-Neutral Research Center, Sungkyunkwan University, Suwon 16419, Republic of Korea

[e]LiB Materials Research Group, Research Institute of Industrial Technology and Science (RIST), POSCO Global R&D Center, Songdogwahak-ro 100, Yeonsu-gu, Incheon, 21985, Republic of Korea. E-mail: omkwon0823@posco-inc.com

† Electronic supplementary information (ESI) available. See DOI: https://doi.org/10.1039/d5ta02205c

‡ These authors contributed equally to this work.

This journal is © The Royal Society of Chemistry 2025

J. Mater. Chem. A, 2025, **13**, 16547–16555 | 16547

mixture of various cation and anion substitutions in argyrodites increased conformational entropy and facilitated inter-cage jumps, achieving an ionic conductivity of 13.2 mS cm^{-1} for Li[P$_{0.25}$Si$_{0.25}$Ge$_{0.25}$Sb$_{0.25}$]S$_5$I[21] and 14.05 mS cm^{-1} for Li$_{6.67}$[P$_{0.16}$Si$_{0.16}$Ge$_{0.5}$Sb$_{0.16}$]S$_5$I.[25]

Ionic substitutions have enhanced the ionic conductivity of argyrodite SEs, but they introduce trade-offs, including higher costs due to expensive metals, increased weight from heavy elements, incompatibility with the Li anode, and more complex fabrication processes due to additional elements. Therefore, conventional Li$_6$PS$_5$Cl and its Cl-rich phases, Li$_{6-x}$PS$_{5-x}$Cl$_{1+x}$, have regained attention due to their low cost, good compatibility in ASSBs, and a high ionic conductivity of approximately 10 mS cm^{-1}. Various compositions have been investigated, and increasing disorder in high-entropy phases effectively enhances ionic conductivity.[14] However, the Li-ion conduction mechanism in high-entropy Li$_6$PS$_5$Cl and Li$_{6-x}$PS$_{5-x}$Cl$_{1+x}$ argyrodites has yet to be fully elucidated through computational analysis. Although several theoretical studies have analyzed Li-ion migration in high-entropy argyrodites,[26–28] a comprehensive investigation of the detailed composition of high-entropy phases has not been conducted.

In this study, machine-learned interatomic potentials (MLIPs) were utilized to investigate high-entropy argyrodites. The lithium-ion conduction mechanisms in high-entropy argyrodites were systematically investigated, while comprehensive maps of ionic conduction across detailed compositions were generated using MLIPs. The calculation results show that higher entropy, achieved by increasing S/Cl site inversion in Li$_6$PS$_5$Cl, facilitates long-range Li-ion migration, with maximum ionic conductivity at 50% site inversion. Site energy distribution analysis revealed that increased anion disorder broadens the potential energy landscape, enhancing inter-cage migration. Additionally, high-entropy argyrodites with excess Cl incorporation exhibit a sharp decline in Li-ion conductivity beyond the critical threshold, indicating the additional impact of Li vacancies on conductivity. Overall, this study efficiently analyzed the conduction mechanism in high-entropy argyrodites using MLIPs, demonstrating their reliability and effectiveness in investigating and designing novel superionic conductors.

2. Methods

First-principles calculations were performed using density functional theory (DFT) as implemented in the Vienna *ab initio* Simulation Package.[29] The projector augmented wave method[30] and the generalized gradient approximation with the Perdew–Burke–Ernzerhof functional[31] were used for the calculations. A plane-wave cutoff energy of 550 eV was used for the plane-wave basis, and the k-point grids included a k-point density of at least 1000 per atom. Ionic position relaxations were conducted until the force was less than 0.03 eV Å^{-1}, while the electronic self-consistency loops were converged to a value of 10^{-5} eV. The simulation cells were generated based on the experimental structural configurations. *Ab initio* molecular dynamics (AIMD) simulations were conducted to evaluate Li-ion diffusivity,

employing an NVT ensemble with a Nosé–Hoover thermostat, an energy cut-off of 350 eV, and a Γ-point-only k-point grid.

The Moment Tensor Potential (MTP) formalism was used to obtain machine-learned interatomic potentials (MLIPs) from AIMD simulations.[32–35] AIMD calculations were performed for crystalline and amorphous argyrodite phases (Li$_{6-x}$PS$_{5-x}$Cl$_{1+x}$, x = 0, 0.5, 1.0), elemental phases (Li, P, and S), and lithium binary halide (LiCl). For the crystal argyrodite phases, all possible site disorders between the 4a and 4d sites were considered, and the structure with the lowest energy was used for the AIMD calculations, while fully ordered Li$_6$PS$_5$Cl and Li$_{5.5}$PS$_5$Cl$_{1.5}$ structures were also included. AIMD calculations for the crystal argyrodite phases were performed at four different temperatures (300, 600, 900, and 1200 K) and at three strain levels (−5%, 0%, and 5%). After the heating step (0.5 K fs^{-1}) and equilibration (20 ps at the target temperature), an additional 10 ps of simulations were run, with snapshots extracted every 0.1 ps. This resulted in a total of 1200 training structures (100 snapshots × 4 temperatures × 3 strains) for each crystal argyrodite phase. Amorphous argyrodite structures were also obtained using a melt-and-quench process at three strain levels (−5%, 0%, and 5%), which involved a pre-melting step at 4000 K for 10 ps, melting at 2000 K for 20 ps, and quenching to 300 K for 17 ps at a rate of 100 K ps^{-1}. The structure snapshots were extracted every 0.1 ps during the melting and quenching steps, resulting in a total of 1110 training structures (370 snapshots × 3 strains). Additionally, AIMD calculations for elemental phases and lithium binary halide were performed by increasing the temperature to 1000 K. After the heating step (0.5 K fs^{-1}) to 300 K and 10 ps of equilibration at 300 K, structure snapshots were extracted every 0.2 ps during the heating to 1000 K for 42 ps.

Single-point DFT static calculations were performed using the optB88-vdW functional for the training structures. Using DFT static calculation results from 11 550 argyrodite and 840 precursor structures, the MTP training was performed for the Li–P–S–Cl four-element system for Li$_{6-x}$PS$_{5-x}$Cl$_{1+x}$ argyrodites. The MTP training was performed with a cutoff radius of 6 Å and a maximum level of 10, using fitting weights of 100 : 1 : 0.01 for energy, force, and stress, respectively. The MTP training was validated using the mean absolute errors (MAEs) of total energies, forces, and stresses. A schematic workflow of the MTP training process is illustrated in Fig. S1.†

Classical molecular dynamics (MD) simulations were performed using the trained interatomic potentials with the Large-scale Atomic/Molecular Massively Parallel Simulator (LAMMPS) package.[36] The MD simulations were performed on 4 × 4 × 4 supercell structures under the NPT ensemble for 10 ns at target temperatures. The mean squared displacement (MSD) of Li ions over time was calculated to determine the diffusion coefficient, D,

$$D = \frac{1}{2dt}\left\langle [r(t+t_0) - r(t_0)]^2 \right\rangle \tag{1}$$

where d represents the dimensionality of the system, t_0 is the initial time, and the angled bracket indicates an average over all Li ions. The ionic conductivity, σ, was calculated using the Nernst–Einstein equation.

16548 | *J. Mater. Chem. A*, 2025, **13**, 16547–16555

This journal is © The Royal Society of Chemistry 2025

$$\sigma = \frac{(ze)^2 cD}{k_B T} \qquad (2)$$

where z is the valence of the ion, c is the ion concentration, and D is the diffusion coefficient. Li-ion trajectories from MD simulations were collected to visualize Li-ion migration. Isosurfaces of ionic probability densities were plotted relative to the mean ionic probability density. Additionally, the self-part of the van Hove correlation function, $G_S(r, t)$, was calculated from MD simulations to investigate Li-ion diffusion, illustrating the probability of a Li-ion diffusing a distance r from its initial position after a time t.[37]

The configurational entropy, ΔS_{conf}, of the argyrodite phases was calculated using the mole fraction of each atom in the Wyckoff 4a and 4d sites, based on the following equation:

$$\Delta S_{conf} = \Delta S_{4a} + \Delta S_{4d} = -R \left\{ \left(\sum_{i=1}^{N_{4a}} x_i \ln x_i \right) + \left(\sum_{j=1}^{N_{4d}} x_j \ln x_j \right) \right\}$$
$$(3)$$

where R is the gas constant, N_{4a} and N_{4d} are the numbers of anion species in the 4a and 4d sites, respectively, and x_i and x_j are the mole fractions of elements in the 4a and 4d sites, respectively. The ΔS_{conf} of the argyrodite phases was calculated using a $4 \times 4 \times 4$ supercell.

Site energy distributions were calculated to examine the enhancement of ionic conductivity along inter-cage jump sites, using the method described in earlier work.[38] Calculations were carried out using a unit cell, with a Li atom placed on the T2, T4, and T5 Wyckoff sites.[39] A single-point calculation was performed for all sites, while the charge was externally adjusted to maintain neutrality. The calculated site energies were analyzed using kernel density estimation and normalized by dividing by the number of Wyckoff sites.

3. Results

MLIP was obtained for the Li–P–S–Cl four-element system ($Li_{6-x}PS_{5-x}Cl_{1+x}$) and validated by calculating the root mean square errors (RMSEs) of energy and force relative to values obtained using DFT, as shown in Fig. S2.† The RMSEs for energy and force are 7.5 meV per atom and 0.37 eV Å^{-1} for the Li–P–S–Cl system, which are consistent with previously reported values in the literature.[40,41] The MD simulation using MLIPs was performed with supercells of argyrodite structures, following a convergence test of cell size, as shown in Fig. S3.† The MSD value for Li_6PS_5Cl at 300 K was obtained using MLIPs, and it converged as the cell size increased to a $4 \times 4 \times 4$ supercell (3328 atoms), which is consistent with previous studies.[41]

High-entropy argyrodites were achieved through anion disorder between the 4a and 4d sites, as shown in Fig. 1, leading to high ionic conductivity.[16,22,42,43] In the structure of Li_6PS_5Cl without anion disorder (Fig. 1a), Cl occupies the face centered positions of the cube (Wyckoff 4a), while S occupies the PS_4 tetrahedral sites (Wyckoff 16e) and the center of the cage-like Li polyhedron (Wyckoff 4d). The configurational entropy, ΔS_{conf}, for the 4a and 4d sites is zero in the ordered Li_6PS_5Cl structure,

but increases with the mixing of S and Cl across the 4a and 4d sites, as shown in Fig. 1b. The ΔS_{conf} in Li_6PS_5Cl can be further increased by introducing excess Cl, forming $Li_{6-x}PS_{5-x}Cl_{1+x}$ ($0 \le x \le 1$).

The configurational entropy of $Li_{6-x}PS_{5-x}Cl_{1+x}$, arising from S/Cl inversion at the 4a and 4d sites, generally falls within the medium entropy range ($1 R \le \Delta S_{conf} < 1.5 R$). Achieving higher configurational entropy values beyond 1.5 R would require additional multi-element substitutions involving both cation and anion sites.[16,22] Nevertheless, this study focuses on anion-disordered $Li_{6-x}PS_{5-x}Cl_{1+x}$, where configurational entropy is maximized through S/Cl site inversion, and the system approaches the high entropy threshold 1.5 R. Using the MLIP, Li-ion conduction was systematically investigated with anion disorder at the 4a and 4d sites, while the entropy term was thoroughly incorporated to better understand the role of disorder degree in achieving high conductivity.

The thermodynamic phase stability of high-entropy argyrodites was assessed by calculating the energy above the convex hull for $Li_{6-x}PS_{5-x}Cl_{1+x}$ phases with varying degrees of S/Cl site inversion. As shown in Fig. S4,† the phase stability decreases as the degree of site inversion increases, suggesting that a high degree of inversion may be thermodynamically unfavorable. Notably, argyrodites with maximized configurational entropy were found to be metastable, indicating that such phases may still be experimentally accessible under favorable synthesis conditions.

Li-ion migration in Li_6PS_5Cl under different degrees of anion disorder was investigated using MLIP for the supercell system, as shown in Fig. 2 and S5.† The isosurfaces of the Li-ion probability densities were plotted to visualize the Li-ion trajectories during a 10 ns molecular dynamics (MD) simulation at 300 K. The structure of Li_6PS_5Cl without anion disorder in Fig. 2a (corresponding to zero ΔS_{conf}) exhibited localized Li-ion migration with negligible inter-cage jumps. As the degree of S/Cl site inversion increases to 25% and further to 50% (Fig. 2b and c, respectively), the Li-ion trajectories become more interconnected between the cages, suggesting long-range Li diffusion that results in high ionic conductivity. The substitution of Cl with S at the 4d site weakens the electrostatic attraction with adjacent Li ions, enabling greater Li mobility and facilitating migration to neighboring cages.

As the degree of S/Cl site inversion increases to 75% and further to 100% (indicating that the 4d sites are predominantly occupied by Cl), the Li-ion trajectories become less connected between cages, indicating a decrease in ionic conductivity. With the substitution of Cl at the 4d sites exceeding 50%, the electrostatic attraction is further weakened, leading to expanded cages and a transformation in their shape. At 100% S/Cl site inversion, all 4d sites are occupied by Cl, leading to localized Li-ion migration, with Li ions appearing to occupy more ordered sites (Fig. 2d). This phenomenon is closely related to the entropy arising from anion disorder between the 4a and 4d sites. The ΔS_{conf} is maximized by mixing 50% of Cl with S at the 4d sites in Li_6PS_5Cl, which exhibits the most active inter-cage jumps. The decrease in ΔS_{conf} leads to more ordered

This journal is © The Royal Society of Chemistry 2025

J. Mater. Chem. A, 2025, **13**, 16547–16555 | **16549**

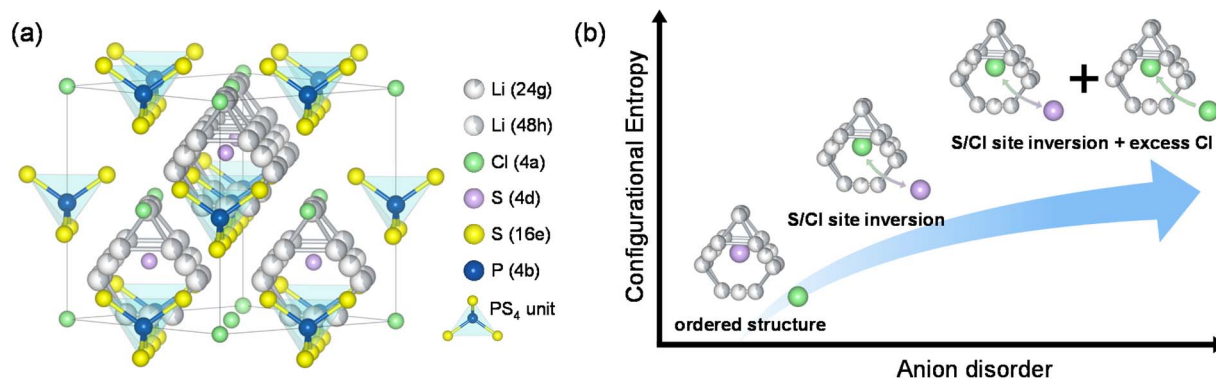**Fig. 1** (a) Crystal structure of argyrodite Li_6PS_5Cl, where Cl occupies the face-centered cubic sites (4a), and S occupies the PS_4 tetrahedral sites (16e) and the center of the cage-like polyhedron (4d) and (b) enhancement of configurational entropy through anion disorder at the 4a and 4d sites.

arrangements, causing Li ions to remain localized at low-energy sites, thereby restricting their migration to adjacent sites.

The detailed analysis of the ionic conduction mechanism as a function of ΔS_{conf} induced by anion disorder was conducted using MLIP, as shown in Fig. 3. Li-ion conductivity in Li_6PS_5Cl was calculated using a 10 ns MD simulation at 300 K by varying the S/Cl site inversion from 0% to 100% in 3.125% intervals, as shown in Fig. 3a. Li-ion conductivity increases as the degree of site inversion increases, reaching a maximum of approximately 15 mS cm^{-1} near 50% site inversion, and declines with further inversion. As predicted by the Li-ion migration trajectories in Fig. 2, higher ΔS_{conf} resulting from S and Cl mixing at the 4a and 4d sites facilitates Li-ion migration, achieving the highest ionic conductivity at the maximum ΔS_{conf}. In Fig. 3b, Li-ion conductivity is plotted as a function of ΔS_{conf}, with the color of each data point corresponding to that in Fig. 3a. As ΔS_{conf} increases, ionic conductivity increases linearly, indicating a strong correlation between ionic conductivity and ΔS_{conf} in Li_6PS_5Cl.

The self-part of the van Hove correlation function, G_s, was calculated for Li_6PS_5Cl to analyze Li-ion migration with increasing S/Cl site inversion, as shown in Fig. 3c. Most Li ions remain near their initial positions in the absence of disorder, and intra-cage jumps of approximately 3 Å are observed, as shown in Fig. 3c. As the degree of S/Cl site inversion increases, the transition to larger r values occurs more rapidly, indicating long-range Li-ion migration (>5 Å) through inter-cage jumps. The G_s values are presented as a function of the degree of site inversion in Fig. S6,† indicating that increasing anion disorder facilitates Li-ion migration across the cage, resulting in higher ionic conductivity. The occurrence of larger r values in the G_s plot decreases above 50% site inversion, confirming the reduction in Li-ion conductivity beyond the maximum entropy point shown in Fig. 3a. The G_s plot for Li_6PS_5Cl with 100% S/Cl site inversion, where all 4d sites are occupied by Cl, verifies the low ionic conductivity by demonstrating localized Li-ion migration.

High ionic conductivity was achieved through long-range Li-ion migration *via* inter-cage jumps, as illustrated in Fig. 4a, including direct inter-cage jumps between T2 sites and inter-cage jumps between T5 sites through the intermediate T4 site.
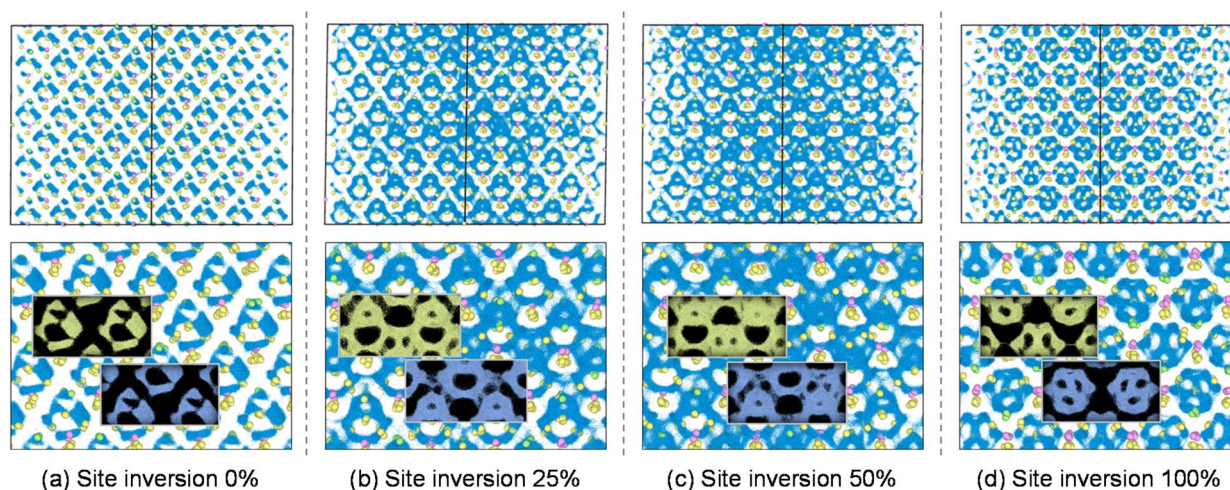

Fig. 2 Isosurfaces of the Li-ion probability densities (light blue) for Li_6PS_5Cl with site disorder between the 4a and 4d sites, shown at different degrees of S/Cl site inversion of (a) 0%, (b) 25%, (c) 50%, and (d) 100%. The top row includes Li (white), P (pink), S (yellow), and Cl (green) atoms, while the bottom row displays only the Li-ion trajectories.
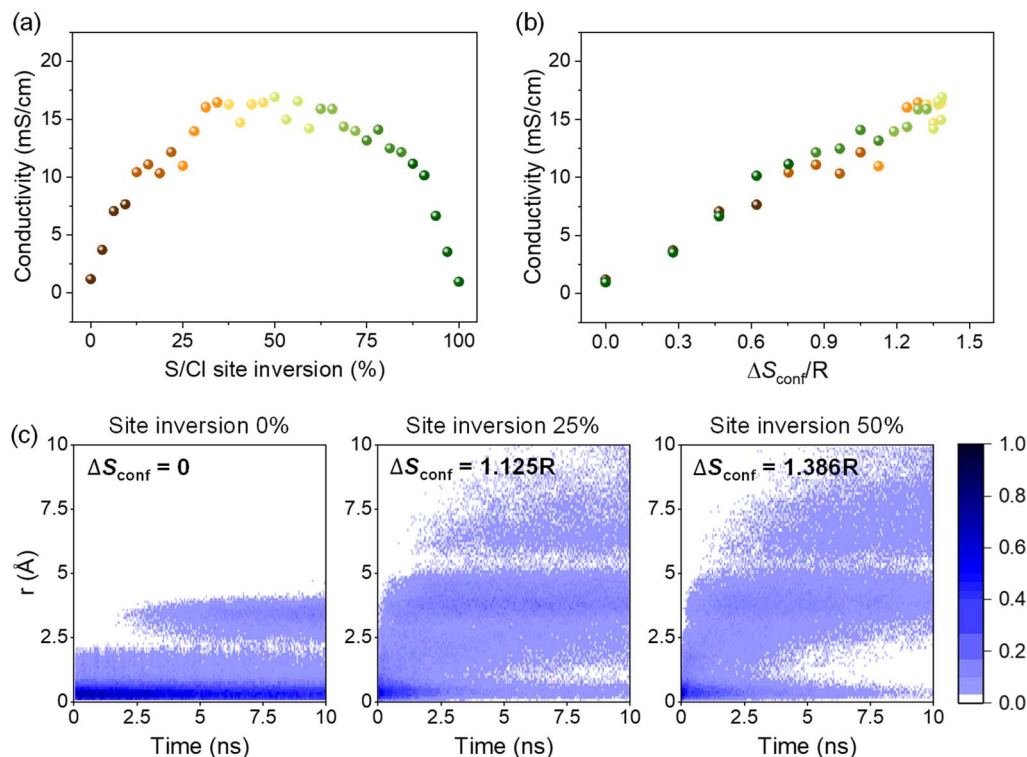
16550 | *J. Mater. Chem. A*, 2025, **13**, 16547–16555

This journal is © The Royal Society of Chemistry 2025

Fig. 3 Li-ion conductivity in Li_6PS_5Cl as a function of S/Cl site inversion between the 4a and 4d sites. Ionic conductivity as a function of (a) the degree of S/Cl site inversion and (b) configurational entropy. (c) The self-part of the van Hove correlation function with increasing degrees of S/Cl site inversion: 0%, 25%, and 50%.
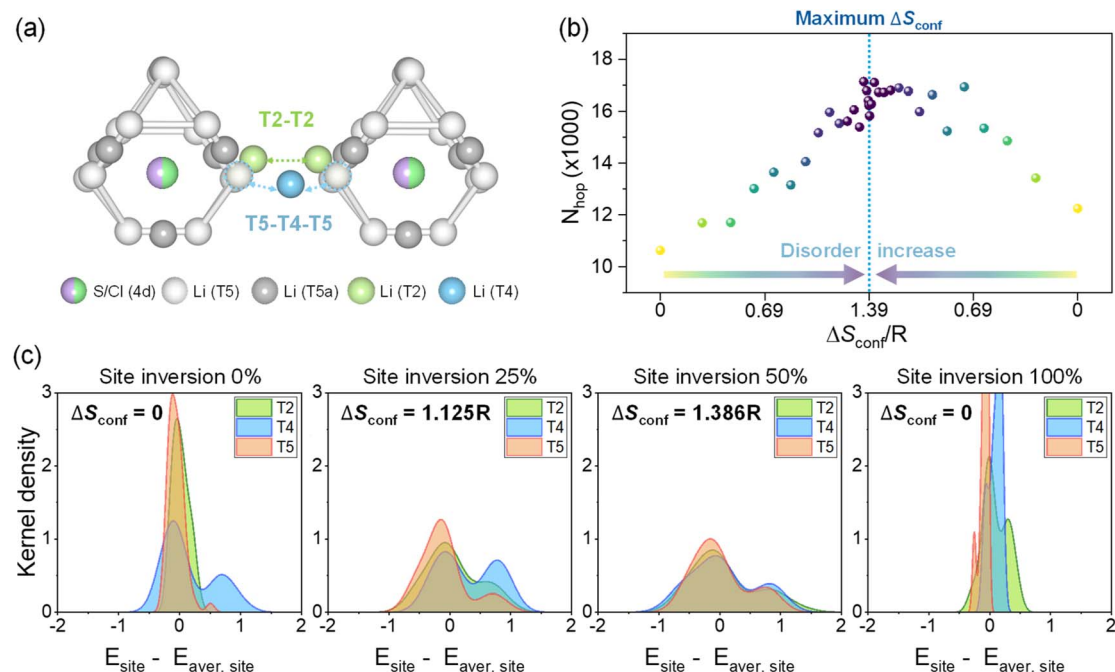

Fig. 4 (a) Illustration of inter-cage jump sites in Li_6PS_5Cl and (b) the number of Li-ion hops between 4d cages as a function of configurational entropy, during the increase in the degree of S/Cl site inversion from 0% to 100%. (c) Site energy distributions for Li at the T2, T4, and T5 sites at different degrees of S/Cl site inversion: 0%, 25%, 50%, and 100%.

This journal is © The Royal Society of Chemistry 2025

J. Mater. Chem. A, 2025, **13**, 16547–16555 | **16551**

Inter-cage jumps were directly counted during the MD simulations, where Li-ion displacements exceeding 3 Å from their initial positions were considered transitions between distinct cages, as shown in Fig. 4b. The frequency of inter-cage Li-ion hopping was examined as a function of ΔS_{conf} to assess the effect of configurational disorder on long-range Li-ion mobility. During the 10 ns MD simulation at 300 K, the number of Li-ion hops to adjacent sites was measured at various degrees of S/Cl site inversion. Consistent with the G_s plots in Fig. 3c and S6,† Li_6PS_5Cl with low anion disorder exhibits fewer Li-ion hops compared to systems with higher disorder, due to restricted migration within intra-cage regions. The number of Li-ion hops increases with greater anion disorder, reaching its maximum at the highest value of ΔS_{conf}, suggesting that additional Li-ion hops are facilitated through inter-cage jumps in high-entropy systems.

The enhanced Li-ion migration at high ΔS_{conf} was further investigated by analyzing the site energy distributions in the structure, using a method previously employed to examine ionic conduction through site disorder.[38,44] Site energy distributions of Li ions along the inter-cage migration paths (T2, T4, and T5 sites) were calculated by varying the degree of S/Cl site inversion, as shown in Fig. 4c and S7.† The site energy distribution describes the potential energy of Li ions along their migration sites and is limited to a narrow region when the sites are more ordered and exhibit lower energy. The site energy distribution broadens as disorder is introduced, due to the more uniform potential energy landscape of Li ions resulting from increased site similarity caused by the disorder. In the site energy

distribution for low anion disorder with low ΔS_{conf}, the site energy of each site exhibits a distinct and narrow region with reduced overlap. However, the site energy distributions for the T2, T4, and T5 sites begin to overlap as ΔS_{conf} increases, allowing Li ions to experience a more continuous energy landscape with lowered barriers to migrate to other sites. The site energy distributions exhibit the greatest overlap at the maximum ΔS_{conf}, indicating that Li-ion migration can be substantially enhanced in this state.

High-entropy argyrodites formed by anion disorder in Li_6PS_5Cl significantly increase ionic conductivity, and further enhancement of entropy can be achieved through excess chlorine incorporation, forming $Li_{6-x}PS_{5-x}Cl_{1+x}$ ($0 \leq x \leq 1$). Using MLIP, Li-ion conduction in Cl-rich phases was investigated as a function of the degree of S/Cl site inversion, as shown in Fig. 5. The ΔS_{conf} values were calculated as a function of additional Cl in $Li_{6-x}PS_{5-x}Cl_{1+x}$ ($0 \leq x \leq 1$, with an interval of 0.125), as shown in Fig. 5a, assuming that the additional Cl occupies the 4d sites (e.g., for $Li_{5.5}PS_{4.5}Cl_{1.5}$ with an additional 0.5 Cl, at least 0.5 Cl can be positioned at the 4d sites, indicating a minimum of 50% S/Cl site inversion). For each composition, ΔS_{conf} was calculated by varying the degree of S/Cl site inversion in 12.5% intervals, starting from the minimum site inversion value. For example, Li_6PS_5Cl was evaluated over nine site inversion degrees from 0% to 100%, while $Li_{5.5}PS_{4.5}Cl_{1.5}$ was evaluated over five site inversion degrees from 50% to 100%. In Fig. 5a, the ΔS_{conf} values were presented as a bar chart for each composition, showing the maximum and minimum values, with green bars representing the 25% to 75% range and the average values indicated by a red line. The ΔS_{conf} increases with additional
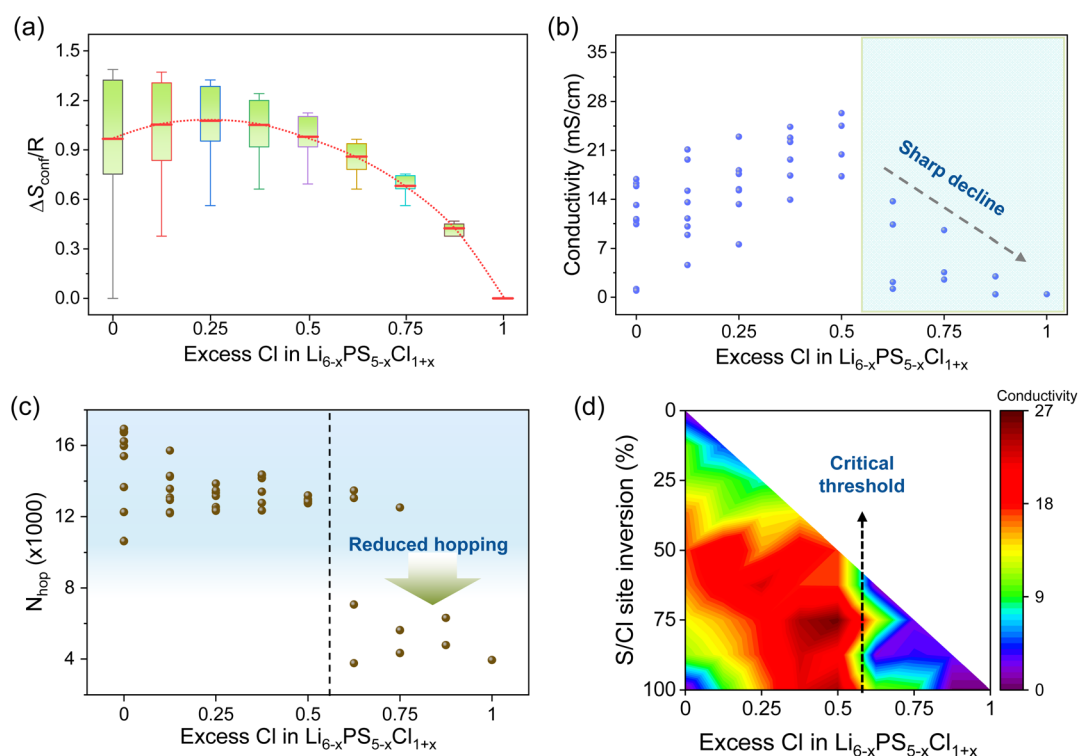

Fig. 5   (a) Configurational entropy, (b) ionic conductivity, and (c) the number of Li-ion inter-cage hops for Cl-rich argyrodites $Li_{6-x}PS_{5-x}Cl_{1+x}$ ($0 \leq x \leq 1$) as a function of Cl content with varying degrees of S/Cl site inversion. (d) The contour map of ionic conductivity shown in (b).
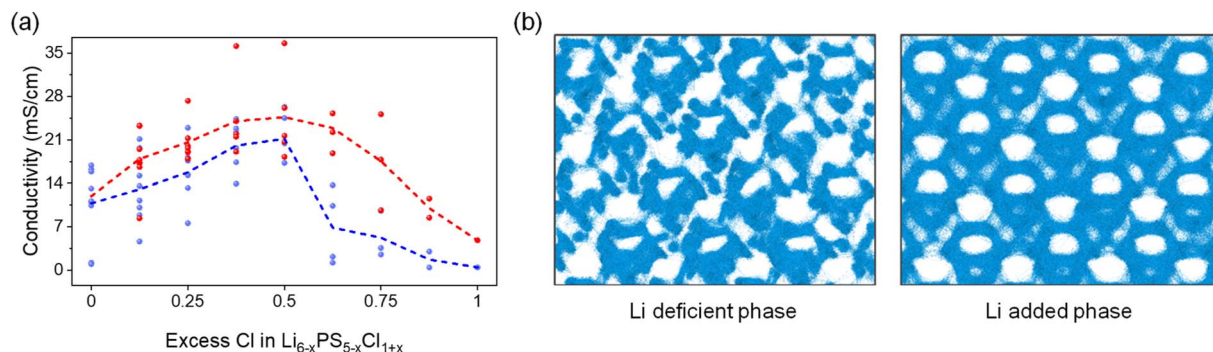
16552 | J. Mater. Chem. A, 2025, 13, 16547–16555

This journal is © The Royal Society of Chemistry 2025

Fig. 6 (a) Ionic conductivities of the Li-deficient phase (blue) and Li-added phase (red) for Cl-rich argyrodites $Li_{6-x}PS_{5-x}Cl_{1+x}$. (b) Isosurfaces of the Li-ion probability densities after Li addition ($Li_6PS_{4.375}Cl_{1.625}$) in the Li-deficient phase $Li_{5.375}PS_{4.375}Cl_{1.625}$ ($x = 0.625$).

Cl incorporation up to $x = 0.25$ and exhibits a slight decline beyond this point, while it significantly decreases above $x = 0.5$, as most 4d sites become occupied by Cl, thereby reducing disorder.

The effect of ΔS_{conf} on Li-ion migration was further investigated for Cl-rich phases using MD simulations at 300 K for 10 ns, as shown in Fig. 5b–d. The MD calculations were performed for compositions in $Li_{6-x}PS_{5-x}Cl_{1+x}$ ($0 \leq x \leq 1$, with an interval of 0.125), with the degree of S/Cl site inversion varied in 12.5% intervals, starting from the minimum site inversion value. In Fig. 5b, Li-ion conductivity increases with a small amount of additional Cl incorporation, consistent with the trends of ΔS_{conf} with increasing Cl content, indicating that enhanced disorder facilitates Li-ion migration. Li-ion conductivity increases with additional Cl incorporation, reaching a maximum near the composition of $x = 0.5$ ($Li_{5.5}PS_{4.5}Cl_{1.5}$). As the Cl content increases to $x = 0.5$, the increase in entropy facilitates more active inter-cage jumps, while the formation of Li vacancies due to additional Cl further reduces the activation barrier for Li migration.[45] Beyond $x = 0.5$, Li-ion conductivity exhibits a sharp decline, consistent with previous experimental studies.[46,47] This pronounced decline contrasts with the gradual decreasing trend of ΔS_{conf} in Fig. 5a, indicating that ΔS_{conf} is not the only factor influencing Li-ion conductivity, as additional Li vacancies also play a role. The Li vacancies formed by Cl incorporation in $Li_{6-x}PS_{5-x}Cl_{1+x}$ can reduce the extent of concerted Li-ion migration by removing Li ions from the migration pathways, leading to a substantial decrease in ionic conductivity.

In Fig. 5c, Li-ion hopping was further examined to investigate the significant decline in ionic conductivity in Cl-rich phases. The Li-ion hopping away from its initial position to neighboring sites (jump length > 3 Å) was counted during MD simulations for Cl-rich phases. As predicted from the low ionic conductivity in Cl-rich phases, the number of Li-ion hops substantially decreases with compositions with more than 0.5 additional Cl incorporation. Therefore, Li vacancies, along with the level of Cl incorporation, are important factors in achieving high ionic conductivity in $Li_{6-x}PS_{5-x}Cl_{1+x}$. In Fig. 5d and S8,† the ionic conductivity data from Fig. 5b are presented in detail as functions of both Cl incorporation and the degree of S/Cl site inversion, using a heat map and a contour map. The contour map in Fig. 5d visually displays a region of reduced ionic conductivity, with a critical threshold at 0.5 Cl incorporation.

The effects of Li vacancies on ionic conductivity in Cl-rich phases were further investigated by restoring the deficient Li, as shown in Fig. 6a. For Li-deficient phases $Li_{6-x}PS_{5-x}Cl_{1+x}$, Li-ion conductivity slightly increases with Cl content, reaching a maximum at $x = 0.5$, and then decreases sharply (shown as blue dots and line). After Li compensation in the phases Li_6-$PS_{5-x}Cl_{1+x}$, the Li-ion conductivity exhibits similar trends, but the curves show a gradual change without a significantly reduced region (shown as red dots and line). The scattered ionic conductivity values for each composition result from variations in the degree of S/Cl site inversion, whereas the averaged values exhibit a more coherent behavior. These ionic conductivities show a stronger correlation with the trend of ΔS_{conf} in Fig. 5a, compared to the ionic conductivity of Li-deficient phases. These findings suggest that the ΔS_{conf} resulting from anion disorder in Cl-rich phases can be a significant factor in determining ionic conductivity, while additional Li vacancies introduced by Cl incorporation also affect Li-ion migration, particularly exhibiting a critical threshold for ionic conductivity in Li-deficient phases above $x = 0.5$.

The improved ionic conductivity through Li vacancy compensation was analyzed using the isosurfaces of the Li-ion probability densities, as shown in Fig. 6b. The Li-ion trajectories for the Li-deficient phase $Li_{5.375}PS_{4.375}Cl_{1.625}$ ($x = 0.625$) were obtained during 10 ns MD simulations at 300 K and compared with those of the Li-added phase $Li_6PS_{4.375}Cl_{1.625}$. Consistent with the ionic conductivities in Fig. 6a, the Li-deficient phases exhibit more fragmented Li-ion trajectories along the migration paths, suggesting a weakening of concerted Li-ion migration due to Li vacancies. In contrast, the modified phases with restored Li vacancies exhibit more connected Li-ion trajectories, consistent with the enhanced ionic conductivity. Additionally, the radial distribution function (RDF) plot in Fig. S9† indicates that the bonds of Li with Cl in the 4d cages become less localized at a specific length and shift to larger values after Li replenishment, suggesting that Li ions are weakly bonded to the cages, thereby facilitating their movement.

4. Conclusions

High-entropy argyrodites with anion disorder have emerged as promising superionic conductors; however, the details of the Li-

This journal is © The Royal Society of Chemistry 2025

J. Mater. Chem. A, 2025, **13**, 16547–16555 | **16553**

ion conduction mechanism have yet to be fully elucidated. In this study, the Li-ion conduction mechanism is systematically investigated through first-principles calculations and molecular dynamics simulations using MLIPs. The calculation results show that increasing S/Cl site inversion in Li_6PS_5Cl enhances inter-cage connectivity and long-range diffusion. Higher ΔS_{conf} facilitates long-range Li-ion migration, with maximum ionic conductivity at 50% S/Cl site inversion, while excessive inversion leads to localization and reduced conductivity. Site energy distribution analysis revealed that increased anion disorder broadens the potential energy landscape and causes site energy overlap, which results in lower migration barriers and enhanced inter-cage migration.

In addition, high-entropy argyrodites with excess Cl incorporation in $Li_{6-x}PS_5Cl_{1+x}$ ($0 \leq x \leq 1$) were investigated, revealing that ΔS_{conf} initially increased but then dropped significantly due to Cl saturation at 4d sites. Li-ion conductivity followed a similar trend, sharply declining beyond the critical threshold of $x = 0.5$, indicating the additional impact of Li vacancies on conductivity. After Li compensation in $Li_{6-x}PS_5Cl_{1+x}$, Li-ion conductivity changes more gradually without a significantly reduced region and shows a stronger correlation with ΔS_{conf}, indicating that anion disorder is a key factor in ionic conductivity, while Li vacancies introduced by Cl incorporation also play an important role. Overall, a detailed analysis of the conduction mechanism in high-entropy argyrodites was efficiently conducted using MLIPs. This study highlights the reliability and effectiveness of MLIPs in guiding the design and analysis of novel high-entropy superionic argyrodites.

Data availability

The data supporting this article have been included as part of the ESI.†

Author contributions

Myeongcho Jang: conceptualization, formal analysis, investigation, and writing – original draft. Kanguk Park: investigation, visualization, and methodology. Hun-Gi Jung: investigation. Kyung Yoon Chung: resources. Joon Hyung Shim: supervision. Ohmin Kwon: supervision. Seungho Yu: conceptualization, supervision, and writing – review & editing.

Conflicts of interest

There are no conflicts to declare.

Acknowledgements

References

1 Y. Tian, G. Zeng, A. Rutt, T. Shi, H. Kim, J. Wang, J. Koettgen, Y. Sun, B. Ouyang, T. Chen, Z. Lun, Z. Rong, K. Persson and G. Ceder, *Chem. Rev.*, 2020, **121**, 1623–1669.

2 A. Manthiram, X. Yu and S. Wang, *Nat. Rev. Mater.*, 2017, **2**, 1–16.

3 S. Randau, D. A. Weber, O. Kötz, R. Koerver, P. Braun, A. Weber, E. Ivers-Tiffée, T. Adermann, J. Kulisch, W. G. Zeier, F. H. Richter and J. Janek, *Nat. Energy*, 2020, **5**, 259–270.

4 T. Schmaltz, F. Hartmann, T. Wicke, L. Weymann, C. Neef and J. Janek, *Adv. Energy Mater.*, 2023, **13**, 2301886.

5 J. Wu, S. Liu, F. Han, X. Yao and C. Wang, *Adv. Mater.*, 2021, **33**, 2000751.

6 C. Wang, J. Liang, Y. Zhao, M. Zheng, X. Li and X. Sun, *Energy Environ. Sci.*, 2021, **14**, 2577–2619.

7 L. Zhou, N. Minafra, W. G. Zeier and L. F. Nazar, *Acc. Chem. Res.*, 2021, **54**, 2717–2728.

8 N. Kamaya, K. Homma, Y. Yamakawa, M. Hirayama, R. Kanno, M. Yonemura, T. Kamiyama, Y. Kato, S. Hama, K. Kawamoto and A. Mitsui, *Nat. Mater.*, 2011, **10**, 682–686.

9 L. Zhou, K.-H. Park, X. Sun, F. Lalère, T. Adermann, P. Hartmann and L. F. Nazar, *ACS Energy Lett.*, 2018, **4**, 265–270.

10 R. P. Rao and S. Adams, *Phys. Status Solidi A*, 2011, **208**, 1804–1807.

11 J.-S. Park, C.-H. Jo and S.-T. Myung, *Energy Storage Mater.*, 2023, **61**, 102869.

12 H. J. Deiseroth, S. T. Kong, H. Eckert, J. Vannahme, C. Reiner, T. Zaiß and M. Schlosser, *Angew. Chem., Int. Ed.*, 2008, **120**, 767–770.

13 C. Yu, F. Zhao, J. Luo, L. Zhang and X. Sun, *Nano Energy*, 2021, **83**, 105858.

14 D. Wang, H. Shi, S. Wang, X. Wu, W. Jiang, S. Liang and Z. Xu, *Coord. Chem. Rev.*, 2024, **508**, 215776.

15 W. D. Jung, J.-S. Kim, S. Choi, S. Kim, M. Jeon, H.-G. Jung, K. Y. Chung, J.-H. Lee, B.-K. Kim, J.-H. Lee and H. Kim, *Nano Lett.*, 2020, **20**, 2303–2309.

16 S. Li, J. Lin, M. Schaller, S. Indris, X. Zhang, T. Brezesinski, C. W. Nan, S. Wang and F. Strauss, *Angew. Chem., Int. Ed.*, 2023, **62**, e202314155.

17 S. V. Patel, S. Banerjee, H. Liu, P. Wang, P.-H. Chien, X. Feng, J. Liu, S. P. Ong and Y.-Y. Hu, *Chem. Mater.*, 2021, **33**, 1435–1443.

18 P. Wang, S. Patel, H. Liu, P. H. Chien, X. Feng, L. Gao, B. Chen, J. Liu and Y. Y. Hu, *Adv. Funct. Mater.*, 2023, **33**, 2307954.

19 L. Zhou, A. Assoud, Q. Zhang, X. Wu and L. F. Nazar, *J. Am. Chem. Soc.*, 2019, **141**, 19002–19013.

20 Y. Lee, J. Jeong, H. J. Lee, M. Kim, D. Han, H. Kim, J. M. Yuk, K.-W. Nam, K. Y. Chung, H.-G. Jung and S. Yu, *ACS Energy Lett.*, 2021, **7**, 171–179.

16554 | *J. Mater. Chem. A*, 2025, **13**, 16547–16555

This journal is © The Royal Society of Chemistry 2025

21 J. Lin, G. Cherkashinin, M. Schafer, G. Melinte, S. Indris, A. Kondrakov, J. r. Janek, T. Brezesinski and F. Strauss, *ACS Mater. Lett.*, 2022, **4**, 2187–2194.

22 W. Li, Z. Chen, Y. Chen, L. Zhang, G. Liu and L. Yao, *Adv. Funct. Mater.*, 2024, **34**, 2312832.

23 Y. Li, S. Song, H. Kim, K. Nomoto, H. Kim, X. Sun, S. Hori, K. Suzuki, N. Matsui, M. Hirayama, T. Mizoguchi, T. Saito, T. Kamiyama and R. Kanno, *Science*, 2023, **381**, 50–53.

24 B. Ouyang and Y. Zeng, *Nat. Commun.*, 2024, **15**, 973.

25 J. Lin, M. Schaller, S. Indris, V. Baran, A. Gautam, J. Janek, A. Kondrakov, T. Brezesinski and F. Strauss, *Angew. Chem., Int. Ed.*, 2024, **63**, e202404874.

26 J. Lee, S. Ju, S. Hwang, J. You, J. Jung, Y. Kang and S. Han, *ACS Appl. Mater. Interfaces*, 2024, **16**, 46442–46453.

27 J. H. Kim, B. Jun, Y. J. Jang, S. H. Choi, S. H. Choi, S. M. Cho, Y.-G. Kim, B.-H. Kim and S. U. Lee, *Nano Energy*, 2024, **124**, 109436.

28 P.-H. Chien, B. Ouyang, X. Feng, L. Dong, D. Mitlin, J. Nanda and J. Liu, *Chem. Mater.*, 2023, **36**, 382–393.

29 G. Kresse and J. Furthmüller, *Phys. Rev. B:Condens. Matter Mater. Phys.*, 1996, **54**, 11169.

30 P. E. Blöchl, *Phys. Rev. B:Condens. Matter Mater. Phys.*, 1994, **50**, 17953.

31 J. P. Perdew, K. Burke and M. Ernzerhof, *Phys. Rev. Lett.*, 1996, **77**, 3865.

32 I. S. Novikov, K. Gubaev, E. V. Podryabinkin and A. V. Shapeev, *Mach. learn.: sci. technol.*, 2020, **2**, 025002.

33 J. Li, M. Zhou, H. H. Wu, L. Wang, J. Zhang, N. Wu, K. Pan, G. Liu, Y. Zhang, J. Han, X. Liu, X. Chen, J. Wan and Q. Zhang, *Adv. Energy Mater.*, 2024, **14**, 2304480.

34 R. Jalem, M. L. H. Chandrappa, J. Qi, Y. Tateyama and S. P. Ong, *Energy Adv.*, 2023, **2**, 2029–2041.

35 J. Qi, S. Banerjee, Y. Zuo, C. Chen, Z. Zhu, M. H. Chandrappa, X. Li and S. P. Ong, *Mater. Today Phys.*, 2021, **21**, 100463.

36 A. P. Thompson, H. M. Aktulga, R. Berger, D. S. Bolintineanu, W. M. Brown, P. S. Crozier, P. J. In't Veld, A. Kohlmeyer, S. G. Moore, T. D. Nguyen, R. Shan, M. J. Stevens, J. Tranchida, B. Trott and S. J. Plimpton, *Comput. Phys. Commun.*, 2022, **271**, 108171.

37 Z. Deng, Z. Zhu, I.-H. Chu and S. P. Ong, *Chem. Mater.*, 2017, **29**, 281–288.

38 Y. Zeng, B. Ouyang, J. Liu, Y.-W. Byeon, Z. Cai, L. J. Miara, Y. Wang and G. Ceder, *Science*, 2022, **378**, 1320–1324.

39 S. T. Kong, H. J. Deiseroth, C. Reiner, Ö. Gün, E. Neumann, C. Ritter and D. Zahn, *Chem.–Eur. J.*, 2010, **16**, 2198–2206.

40 J. W. Lee, J. H. Kim, J. S. Kim, Y. J. Jang, S. H. Choi, S. H. Choi, S. M. Cho, Y.-G. Kim and S. U. Lee, *J. Mater. Chem. A*, 2024, **12**, 7272–7278.

41 H. J. Lee, H. Kim, S. Ji, K. Choi, H. Choi, W. Lim and B. Lee, *Adv. Energy Mater.*, 2024, **14**, 2402396.

42 F. Strauss, J. Lin, A. Kondrakov and T. Brezesinski, *Matter*, 2023, **6**, 1068–1070.

43 H. Guo, J. Li, M. Burton, J. Cattermull, Y. Liang, Y. Chart, G. J. Rees, J. Aspinall and M. Pasta, *Cell Rep. Phys. Sci.*, 2024, **5**, 102228.

44 T. Jeon, G. H. Cha and S. C. Jung, *J. Mater. Chem. A*, 2024, **12**, 993–1002.

45 W. Li, M. Li, S. Wang, P.-H. Chien, J. Luo, J. Fu, X. Lin, G. King, R. Feng, J. Wang, J. Zhou, R. Li, J. Liu, Y. Mo, T.-K. Sham and X. Sun, *Nat. Nanotechnol.*, 2025, **20**, 265–275.

46 Y. J. Choi, S.-I. Kim, M. Son, J. W. Lee and D. H. Lee, *Nanomaterials*, 2022, **12**, 4355.

47 C. Yu, Y. Li, M. Willans, Y. Zhao, K. R. Adair, F. Zhao, W. Li, S. Deng, J. Liang, M. N. Banis, R. Li, H. Huang, L. Zhang, R. Yang, S. Lu, Y. Huang and X. Sun, *Nano Energy*, 2020, **69**, 104396.

This journal is © The Royal Society of Chemistry 2025

J. Mater. Chem. A, 2025, **13**, 16547–16555 | **16555**